

E08014 Cross Section Extraction

Zhihong Ye
University of Virginia

May 26, 2015

Contents

1	Overview	2
2	Beam Charge	3
3	Dead-Time	4
4	Targets	5
4.1	Cryo-Target Boiling Effect	6
5	Detector Efficiencies	7
5.1	Trigger Efficiency	7
5.2	Vertical Drift Chamber Efficiency	8
5.3	Particle Identification Efficiencies	9
6	Monte Carlo Simulation	16
7	Cross Section Model	19
8	Event Selection and Corrections	19
8.1	Central Momentum and Angle	20
8.2	Acceptance Correction	21
8.3	Binning Correction	22
8.4	Cuts	22
9	From Yields to Cross Sections	23
10	Calculation of Errors	24
10.1	Y_{EX} :	24
10.1.1	Statistic Errors	24
10.1.2	Systematic Errors	24
10.2	Y_{MC} :	25
10.2.1	Statistical Errors	25
10.2.2	Systematic Errors	25
10.3	Systematic Table	25
10.4	Systematic Errors in Cross Section Ratio	27

List of Figures

1	Flow-chart illustrating cross section extraction	3
2	Cryo-target bumps	6
3	Trigger efficiency vs run number	8
4	Electron and pion samples from the calorimeters	10
5	Electron and pion samples from the GC	11
6	Cut scan of the GCs	12
7	Cut scan of the calorimeters	13
8	PID cut on the GCs	14

9	PID cut on the calorimeters	15
10	Simulation of ^{12}C target plane quantities	17
11	Simulation of ^3He target plane quantities	18
12	A sketch of cross section lookup tables	19
13	Central momentum deviation	20
14	A demonstration of the acceptance effect	21

1 Overview

Assuming the data is binned in the energy of scattered electrons, E' , the experimental raw cross section can be written as:

$$\frac{d\sigma_{EX}^{raw}}{dE'd\Omega}(E_0, E'_i, \theta_0) = \frac{N_{EX}^i \cdot \epsilon_{e-\pi}}{N_e \cdot \eta_{tg} \cdot \epsilon_{eff} \cdot (\Delta E'_i \Delta \Omega_{EX})}, \quad (1)$$

where the superscript i denotes the i th bin. E_0 is the incident energy set at 3.356 GeV in the E08-014, E'_i is the scattered energy at the center of the bin, and θ_0 is the central scattering angle. $\Delta E'$ and $\Delta\Omega = \Delta\theta_{tg} \cdot \Delta\phi_{tg}$ are the momentum acceptance and the solid angle acceptance of the spectrometer; N_{EX}^i is the number of scattered electron events in this bin; η_{tg} is the areal density of scattering centers; N_e is the total number of electrons in the beam; and ϵ_{eff} is the total efficiency of all detectors combined, including the detection efficiency and the cut efficiency. $\epsilon_{e-\pi}$ corrects for the pion-contamination in the electrons after the PID cuts. In the rest of this chapter, the differential form of the cross section, $\frac{d\sigma}{dE'd\Omega}(E_0, E'_i, \theta_0)$, is abbreviated to $\sigma(E'_i, \theta_0)$.

The raw cross section in Eq. (1) requires additional corrections to remove the effects from the spectrometer acceptance. Also, E_0 and E'_i are altered when the electron loses its energy as it passes through the target due to the radiative effects before and after the scattering (see Appendix B.5). The experimental cross section, usually called the radiated cross section, has to be further corrected for radiative effects. The final cross section is the Born cross section, which can be directly compared with theoretical calculations.

The basic procedure of extracting cross sections from experimental data is demonstrated in Fig. 1. First of all, the signals from detectors and electronics were stored in the raw data in the form of TDC channels, ADC channels and scaler counts. These signals have to be properly calibrated and converted into applicable quantities. The calibrated HRS optics matrix reconstructs the scattered electron's momentum, scattering angle and reaction point at the target plane. The full set of raw data was replayed with updated parameters in the data base. The calibration of detectors and the HRS optics matrices have been introduced in the previous chapter.

Secondly, the results of the beam charge monitor (BCM) calibration convert the BCM scaler counts into electron beam charge. The dead-time associated with the DAQ system needs to be evaluated to recover the events lost during the data acquisition. η_{tg} is determined by the target thickness after the boiling study. Good electrons are identified by applying cuts on calibrated detector signals, and the efficiencies of the event selection can be individually determined. By binning the data with the kinematic variable, e.g. E' , in its proper acceptance range, one can extract the experiment yield in each bin. A description of all the procedures will be given in this chapter.

In addition, the single arm Monte Carlo simulation (SAMC) generates simulation events with the same kinematic settings but with a wider acceptance range to correct the acceptance effect of the HRSs. After weighting the simulation events with the cross sections calculated from model (e.g. XEMC in this experiment), the simulation yields were extracted with the same acceptance cuts and binning method. The Monte Carlo simulation and cross section models will also be discussed in this chapter.

Finally, the yield ratio method used to extract the cross sections will be introduced, followed by a discussion of errors.

The flow-chart to extract inclusive cross sections

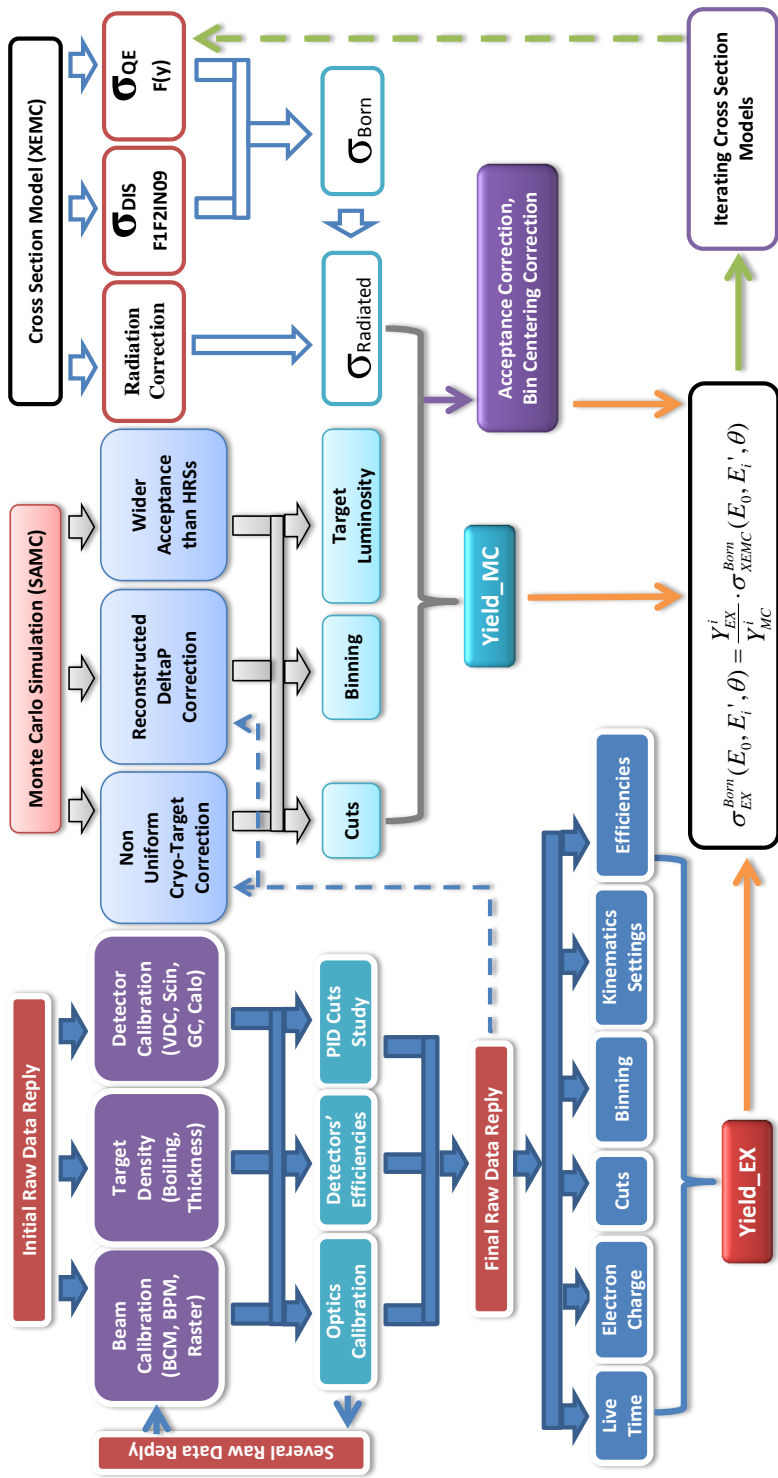


Figure 1: Flow-chart illustrating cross section extraction

2 Beam Charge

The accumulated electron charge from the beam was monitored by BCMs, where signals were recorded in scalers. The scalers signals, in term of number of counts, have been calibrated [1] to correctly reflect the accumulated electron charge. When the beam is stable during one run, the total electron charge is simply the product of the beam current and the total run time, and should be directly proportional to the total number of scaler counts. However, events taken during the

beam trips must be removed by applying a cut on the electron beam current.

The average electron beam current in between two consecutive scaler events, called the real-time current, is calculated from the total electron charge collected between these events divided by the time gap. For example, between the i th and the $i+1$ th event, the real-time current measured by the upstream BCM scaler, U_1 , is given by:

$$I_i^{U_1} = \Delta C_i^{U_1} / \Delta T_i, \quad (2)$$

where $\Delta C_i^{U_1} = C_{i+1}^{U_1} - C_i^{U_1}$ gives the charge accumulated between two scaler events with the time gap, $\Delta T_i = T_{i+1} - T_i$. Similarly, the real-time current measured by the downstream BCM scaler, D_1 , is also calculated. There are other BCM scaler signals, U_3 and U_{10} (D_3 and D_{10}), which basically measure the same charge signal as U_1 (D_1) but with 3 times and 10 times amplification, respectively. Only U_1 and D_1 were used since this experiment required very high currents.

The beam trip cut is applied on the average of these two real-time current values:

$$\frac{1}{2}(I_{i^*}^{U_1} + I_{i^*}^{D_1}) > I_{beam_trip_cut}, \quad (3)$$

where the cut value can be any value between zero (when beam is tripped) and the value slightly below the maximum current. In this analysis, the beam trip cut was chosen to be 50% of the normal beam current. The total charge after the beam trip cut is given as:

$$Q_e = \frac{1}{2} \sum_{i^*} (\Delta C_{i^*}^{U_1} + \Delta C_{i^*}^{D_1}), \quad (4)$$

where i^* means summing over scaler events with beam current I_{i^*} higher than the cut. And the number of electrons in the beam can be calculated as follows:

$$N_e = Q_e / e, \quad (5)$$

with the electron charge, $e = 1.602 \times 10^{-19}$ C.

After the data replay, scaler events are stored in the scaler trees, **RIGHT** for HRS-R and **LEFT** for HRS-L, respectively, and they are synchronized with trigger events in the **T** tree. There are certain number of trigger events recorded between two consecutive scaler events, and these events are assigned the same value of the real-time beam current evaluated between these two scaler events. Consequently, a beam trip cut removes all trigger events in between two scaler events if the real-time current is lower than the cut.

During this experiment, BCM scalers on HRS-L did not work properly. Due to the fact that the scalers on both HRSs recorded the same BCM signals, the real-time current for data taken in HRS-L was calculated with scaler events in HRS-R.

3 Dead-Time

There are two types of dead-time that can cause the loss of events, the electronic dead-time and the computer dead-time. The electronic dead-time comes from the front-end electronics of the DAQ system, which can discard the incoming trigger events while they are busy with processing the current trigger. The computer dead-time is caused by the limitation of computer speed which can lead to the loss of new events when the computer is still writing the current event into the hard disk. Unless the computer is overloaded by processes other than the DAQ system, the computer dead-time is negligible due to the application of high performance computer hardware.

One evaluates the dead-time as the percentage of the trigger events being discarded to the total trigger events in a certain period of time. The value of the dead-time is directly related to the performance of electronics and computers, but also strongly depends on the total trigger rate. Rather than increasing the hardware performance, a typical method to reduce the dead-time is to limit the total trigger rate below a reasonable value by assigning a pre-scale factor to each trigger.

The online dead-time during data taking is monitored by using the electron dead-time monitor module (EDTM) which mixes pulse signals with fixed frequency into TDC signals. Within a certain amount of time, the total number of the pulse signals is known and the dead-time value can be given by calculating the percentage of the pulse signals which are not recorded by the DAQ system. By changing the pre-scale factors before the start of the each run, this value was kept under 30% in this experiment.

The average value of dead-time in each run for the main production triggers was calculated individually during the offline analysis. Although the total number of events recorded by the DAQ system was scaled by the pre-scale factor, their total triggers were counted by scalers, hence the average dead-time for the i th trigger can be given by:

$$DT_{T_i} = 1 - \frac{PS_{T_i} \cdot N_{T_i}^{DAQ}}{N_{T_i}^{Scaler}}, \quad (6)$$

where PS_{T_i} is the pre-scale factor of the trigger. $N_{T_i}^{Scaler}$ and $N_{T_i}^{DAQ}$ are the total number of scaler counts (in **RIGHT** tree for $i = 1$ or **LEFT** tree for $i = 3$) and trigger events (in **T** tree) for each run, respectively. The beam trip cut was applied when calculating $N_{T_i}^{Scaler}$ and $N_{T_i}^{DAQ}$.

A different quantity, live-time ($LT_{T_i} = 1 - DT_{T_i}$), is more commonly used to correct the total number of good events in each run:

$$N_{T_i,EX}^r = PS_{T_i}^r \cdot \frac{N_{T_i}^{r,recorded}}{LT_{T_i}^r}, \quad (7)$$

where r denotes the run number; $PS_{T_i}^r = PS1^r$ for the T_1 trigger on HRS-R and $PS_{T_i}^r = PS3^r$ for the T_3 trigger on HRS-L; $N_{T_i,EX}^r$ and $N_{T_i}^{r,recorded}$ are the number of selected events which create triggers and the number of those events which are recorded by the DAQ system after pre-scaling, respectively. Note that without event selection, e.g. PID cuts, $N_{T_i}^{r,recorded} = N_{T_i}^{r,DAQ}$.

In this experiment, since only events from T_1 (T_3) were used for data analysis on HRS-R (HRS-L), the subscript, T_i , is omitted in any future discussion.

4 Targets

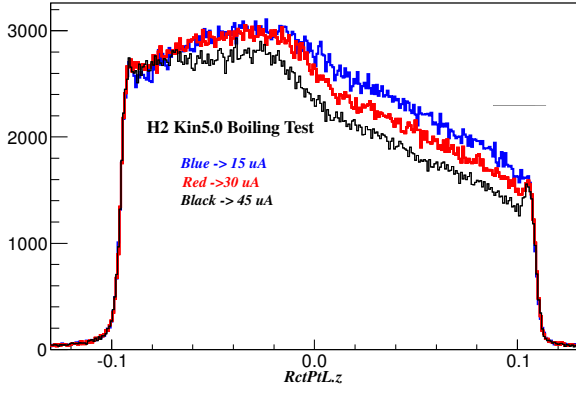
The areal density of scattering centers (in cm^{-2}) in Eq. (1) is calculated from the known target thickness:

$$\eta_{tg} = \frac{\rho \cdot l \cdot N_a}{A}, \quad (8)$$

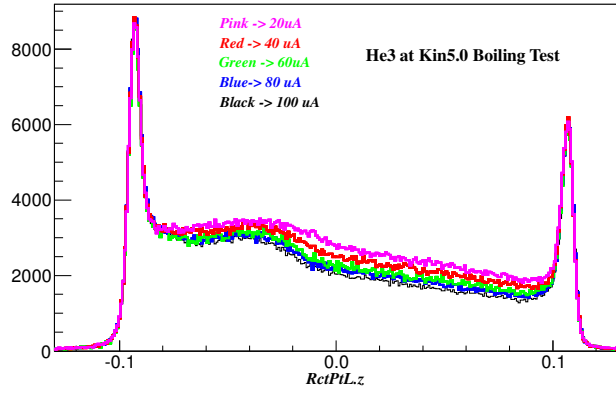
where ρ is the density of the target material in g/cm^3 , l is the effective target length in cm , N_a is the Avogadro's number and A is the nuclear number of the target.

Target	ρ (g/cm ³)	Length (cm)	$\delta\rho$ (g/cm ²)	I (μA)	Comment
LD ₂	0.1676	20.0	N/A	40	Loop2
Al can (Loop-2)	2.7	0.0272	0.0001		Entrance
	2.7	0.0361	0.0011		Exit
	2.7	0.0328	0.0002		Wall
³ He	0.0296	20.0	N/A	120	Loop1
⁴ He	0.0324	20.0	N/A	90	Loop1
Al-can (Loop-1)	2.7	0.0272	0.0002		Entrance
	2.7	0.0361	0.0006		Exit
	2.7	0.0328	0.0005		Wall
¹² C	2.265	0.3937	0.0008	120	
⁴⁰ C	1.55	0.5735	0.01	40	Loop3
⁴⁸ C	1.55	0.5284	0.01	40	Loop3
Al-can (Loop-3)	2.7	0.0272	0.0001		Entrance
	2.7	0.0361	0.001		Exit
	2.7	0.0328	0.0002		Wall
Dummy-20cm	2.7	0.1581	0.0005	40	Upstream
	2.7	0.1589	0.0005		Downstream
Dummy-10cm	2.7	0.1019	0.0003	40	Upstream
	2.7	0.1000	0.0003		Downstream

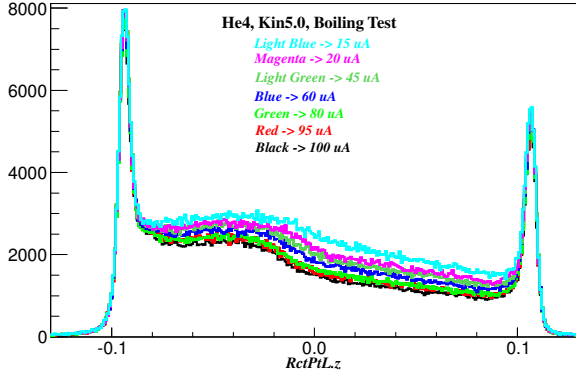
Table 1: Targets in the E08-014, where BeO target and optics target are not listed. The detailed report is in Ref. [2]. The uncertainties of three cryo-targets are needed to be conformed so they are listed temporarily as "N/A".



(a) 2H



(b) 3He



(c) 4He

Figure 2: Cryo-target bumps which appear on the z_{react} distributions because of the non-uniform density of cryo-targets. Due to the boiling effect, the bumps become more significant when the beam current is larger.

4.1 Cryo-Target Boiling Effect

When the electron beam passes through the target, the local temperature fluctuates and causes the target density to vary with the beam current. This phenomenon is called the boiling effect. While the density variation of solid targets is usually negligible, liquid and gas targets have significant boiling effects and their densities correlate to the beam current as follow:

$$\rho = \rho_0 \cdot (1.0 - B \cdot I/100), \quad (9)$$

where I and B are the values of the beam current and the boiling factor for the target, respectively. ρ_0 is the nominal target density at $I = 0$ and ρ is the actual density with the boiling effect.

In the E08-014, three cryogenic targets (cryo-targets), ^2H , ^3He and ^4He , were held in 20 cm long aluminium cells. The cryogenic coolant flowed from the upstream to the downstream of a target cell, and the variation of temperature among different parts of the target leaded to a non-uniform density distribution. When the beam was on, the temperature fluctuation became more significant with higher current. The boiling effect was different along the cryo-target and further increased the non-uniformity of the target densities. Fig. 2 shows the irregular density distribution and the strong correlation between the density and the beam current. The areal density, η_{tg} , for these cryo-targets could not be simply calculated from Eq. (8).

A boiling study was performed by dividing each target into several sections along the cell, where the boiling effect was individually evaluated. The relative density distributions were extrapolated from the boiling study results and the absolute target densities were calculated with the survey report of the target system [2]. A detailed discussion is given in Appendix D.

5 Detector Efficiencies

To extract the electron-scattering cross section, one needs to know the number of scattered electrons coming out from the reaction plane (i.e. the target plane). Every detector is designed to be sensitive to certain types of particles within the known energy ranges. In practice, the detector may not be able to detect everyone of these particles passing through. Each detector has a detection efficiency (ϵ_{det}) which is given as the portion of particles detected to the total. In addition, during the offline analysis, one applies cuts on the reconstructed quantities of the detectors to remove background and select good events, e.g. to identify pure electron events from the target. However, depending on the range of the cut, each cut may also unintentionally discard some good events. The cut efficiency (ϵ_{cut}) denotes the percentage of good events remaining after applying a cut and has to be evaluated when one chooses the value of the cut. In other words, the detection efficiency denotes the survival rate of particles at the hardware level and the cut efficiency represents the level of confidence when selecting good particles at the software level, respectively. In this section, the efficiencies of the HRS detectors will be individually evaluated.

5.1 Trigger Efficiency

The traditional HRS production trigger is generated by the coincidence of logic signals from two scintillator planes (S1 and S2m), so the trigger efficiency is equal to the product of the detection efficiency of these two scintillators. An inefficiency arises when either S1 or S2m does not fire when a particle passes through. As discussed in Section 3.7, T2 (T4) is the trigger generated when only one of S1 and S2m signals coincides with the gas Čerenkov (GC) signal on HRS-R(-L). Using the events from T2 (T4), one can calculate the trigger efficiency of T1 (T3), or equivalently T6 (T7) in the E08-014, as follow:

$$\epsilon_{trig} = \frac{PS1(3) \cdot N_{T1(3)}}{PS1(3) \cdot N_{T1(3)} + PS2(4) \cdot N_{T2(4)}}, \quad (10)$$

where $N_{T1(2,3,4)}$ is number of events triggered by T1(2,3,4) and $PS1(2,3,4)$ is the prescale factor of the trigger.

Note that Eq. (10) is only valid when the GC has 100% detection efficiency. Particles creating T1 (T3) Events ($N_{T1(3)}$) may not necessarily fire the GC, but events from T2 (T4) are recorded when the GC is fired, so $N_{T2(4)}$ has to be corrected by the detection efficiency of the GC. The trigger efficiency should be given by:

$$\epsilon_{trig} = \frac{PS1(3) \cdot N_{T1(3)}}{PS1(3) \cdot N_{T1(3)} + PS2(4) \cdot N_{T2(4)} / \epsilon_{det}^{GC}}, \quad (11)$$

where ϵ_{det}^{GC} is the detection efficiency of the GC. The HRS GCs usually have very high efficiency for detecting electrons, so Eq. (10) is still valid. However, when the efficiency of the GC falls, the trigger efficiency has to be corrected by the detection efficiency of the GC which is evaluated independently.

In the E08-014, as the design of T1 and T3 involved S1, S2m and the GC, hence the trigger efficiency does not depend on the detection efficiency of the GC, which cancels in Eq. (10):

$$\begin{aligned}\epsilon_{trig} &= \frac{PS1(3) \cdot N_{T1(3)} / \epsilon_{det}^{GC}}{PS1(3) \cdot N_{T1(3)} / \epsilon_{det}^{GC} + PS2(4) \cdot N_{T2(4)} / \epsilon_{det}^{GC}} \\ &= \frac{PS1(3) \cdot N_{T1(3)}}{PS1(3) \cdot N_{T1(3)} + PS2(4) \cdot N_{T2(4)}}.\end{aligned}\quad (12)$$

In summary, the assumption that the trigger efficiency is equivalent to the detection efficiency of S1 and S2m is valid only when both T1 (T3) and T2 (T4) involve the logic signal from the GC. The trigger efficiencies of T1 and T3 were calculated individually for each run, shown in Fig. 3.

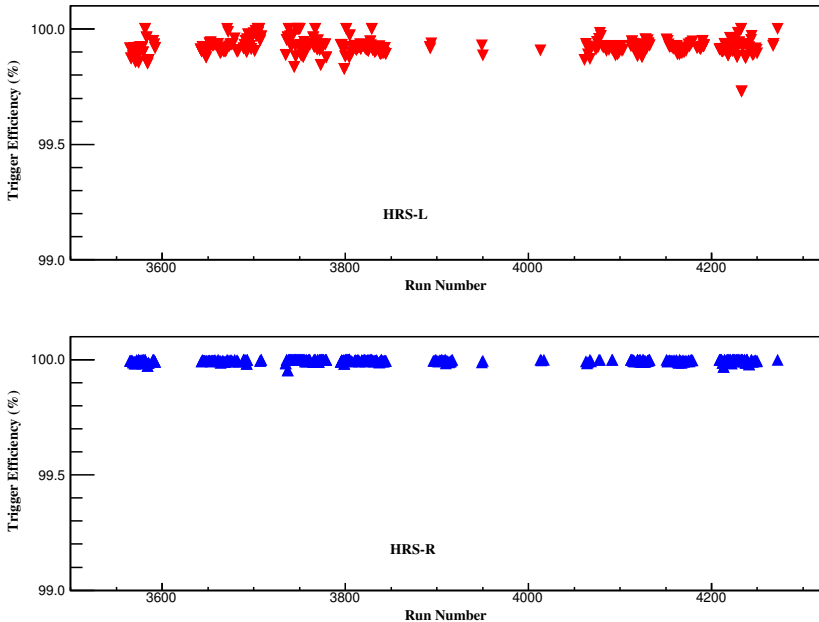


Figure 3: Trigger efficiency vs run number, where the top plot is for T3 trigger on HRS-L and the bottom plot is for T1 trigger on HRS-R.

The results show that the triggers have very high efficiencies.

5.2 Vertical Drift Chamber Efficiency

The detection efficiency of vertical drift chambers (VDCs) is usually very high and the inefficiency is mainly caused by the mis-reconstruction of particle tracks given by the tracking algorithm. Only events with one track were kept for the data analysis, and other events with zero-track and multi-tracks were discarded by applying a one-track-cut. The cut efficiency is generally called the one-track-cut efficiency, which is defined as:

$$\epsilon_{vdc} = \frac{N_{Track=1}}{N_{0 \leq Tracks \leq 4}}, \quad (13)$$

where $N_{Track=1}$ is the number of events with only one track and $N_{0 \leq Tracks \leq 4}$ is the number of events with tracks less than 4. Events with tracks more than 4 are extremely rare for HRS VDCs.

To correctly evaluate ϵ_{vdc} , good electrons were sampled by applying cuts on detector quantities. Those quantities that require tracking information were avoided when selecting electrons — quantities derived from VDCs, the acceptance cuts on the focal plane and the target plane quantities, and the calorimeter's energy sum from the cluster reconstruction. Electrons can be alternately identified by cutting the calibrated ADC sums of the calorimeter and the GC. Events with multi-tracks can also be caused by multiple particles coming in one trigger window, and such events can be eliminated by requiring only one hit in each scintillator plane. Note that because

paddles in S1 partially overlap, good events coming through the overlapped region are discarded when applying such a cut. This cut should be avoided for any other parts of data analysis.

Cosmic ray events usually come into the VDC at large angles and give bad tracking reconstruction, and they can be eliminated by cutting on the time-of-flight velocity (β_{TOF}) calculated from the timing information from S1 and S2m. However, this information was not available in this experiment due to several nonfunctional TDC signals in S1 and S2m, so cosmic ray events were not removed. To suppress the cosmic ray background, data with high trigger rates, such as the carbon target data taken at the kinematic setting at the QE peak, were used to calculate the one-track-cut efficiency. From Table 2, the fraction of one-track and multi-track events are listed, where the one-track efficiency is mostly above 99%. The detection efficiency is the essential property of the detector and should not depend on the kinematic settings, hence one can conclude that the real value of the one-track-cut efficiency is equal to the values calculated with data taken at high rates.

Number of tracks	0	1	2	3	4
HRS-L	0.030%	99.175%	0.743%	0.045%	0.005%
HRS-R	0.048%	99.360%	0.545%	0.039%	0.007%

Table 2: Fraction of different tracks events from QE data,w/o β cut

5.3 Particle Identification Efficiencies

Electrons are identified by the GC and the calorimeter on each HRS. The GC gives high detection efficiency, since the momentum threshold for electrons to create Čerenkov radiation is only 18 MeV/c, while pions and other heavy particles must have their momenta above 4 GeV/c to fire the detectors. The efficiency is mainly related to the performance of the mirrors in the GC to collect and focus the Čerenkov light.

The detection efficiencies of the calorimeters are expected to be lower than the GCs. Each calorimeter is composed of many lead glass blocks, so the inefficiency arises when particles go through gaps between blocks or hit the edges of the calorimeter before it creates a shower.

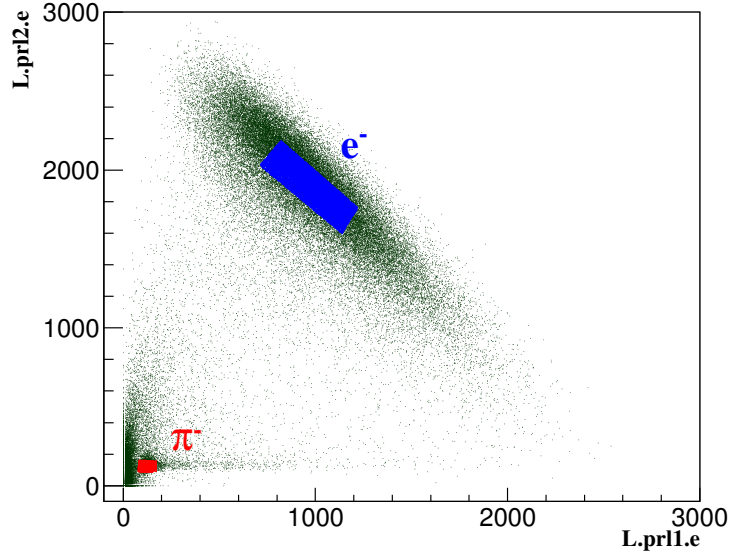
The particle identification (PID) for electrons was performed by applying cuts on the calibrated quantities of the GC and the calorimeter. The cuts can reject most unwanted particles, e.g. pions, but on the other hand, they may also accidentally discard good electrons. The PID study aims to obtain the optimized PID cuts on the GC and the calorimeter which can nearly eliminate pions while keeping as many electrons as possible. The cut efficiencies of the GC and the calorimeter have to be individually evaluated to correct the portion of electrons lost during the cuts.

To evaluate the detection efficiency of the GC (the calorimeter), one first selects electron samples from the calorimeter (the GC) and calculates the percentage of these samples being detected by the GC (the calorimeter), e.g. their signals are slightly larger than the pedestals in the ADC spectrum. Similarly, the evaluation of the cut efficiency for one detector also requires electron samples from the other detectors, but the cut applied on the signals of these samples should be significantly above the pedestals. Hence the calculation of the cut efficiencies for the GCs and the calorimeters should automatically include the detection efficiencies of these detectors.

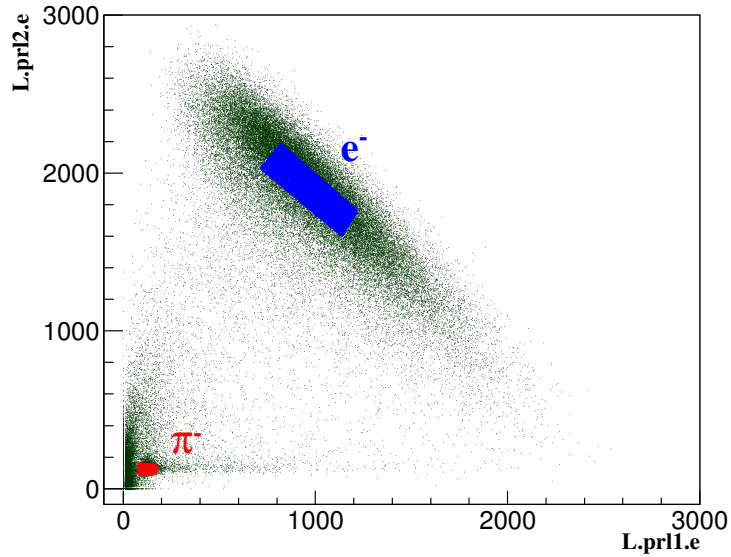
In general, for experiments with a large pion background, evaluating the percentage of residual pions mixed into the electron events ($\epsilon_\pi = 1 - \epsilon_{e-\pi}$) is also very crucial. However, compared with the electron rate in the QE region, the pion production rate during the E08-014 was very low. Additionally, the new trigger design had already removed most of pions during online data taking by introducing the GC in the trigger system. Hence the value of ϵ_π was expected to be very small.

Events from the T6 and T7 triggers were used to study the PID cut efficiencies since they contained the most of pions. The VDC one-track-cut and the acceptance cuts were applied to select good events. Then pure pion samples and pure electron samples were chosen from the calorimeter (GC) when studying the cut efficiency of the GC (calorimeter). The pion rejection efficiency is defined as the percentages of pions removed by applying the PID cuts:

$$\epsilon_{\pi-rej}^{GC(calо)} = \frac{N_\pi^{GC(calо)}}{N_{\pi_samples}^{calо(GC)}}, \quad (14)$$



(a) Pion Rejectors



(b) Pre-Shower and Shower

Figure 4: Electron (blue) and pion (red) samples from the calorimeters. In each plot, the x-axis and the y-axis are the total energies collected by the first layer and the second layer of the calorimeter, respectively. Electrons create large signals either in the first or the second layer during the cascade while the signals created by pions are relatively small in each layer. Graphic cuts were applied on these regions (in color) to select the electrons and pions.

and the electron cut efficiency can be calculated from:

$$\epsilon_{e_cut}^{GC(calо)} = \frac{N_e^{GC(calо)}}{N_{e_samples}^{calо(GC)}}, \quad (15)$$

where $N_{\pi_samples}^{calо(GC)}$ ($N_{e_samples}^{calо(GC)}$) is the pion (electron) samples from the calorimeter (GC) (Fig. 4 and Fig. 5). $N_{\pi}^{GC(calо)}$ is the number of pions rejected and $N_e^{GC(calо)}$ is the number of electrons left over after cutting on the GC (calorimeter), respectively.

A cut scan was performed to study the distributions of the pion rejection efficiencies and the electron cut efficiencies by varying the cuts on the GCs and the calorimeters, shown in Fig. 6 and Fig. 7. Fig. 8a and Fig. 8b show that for the GC, a cut at the low channel value of the calibrated

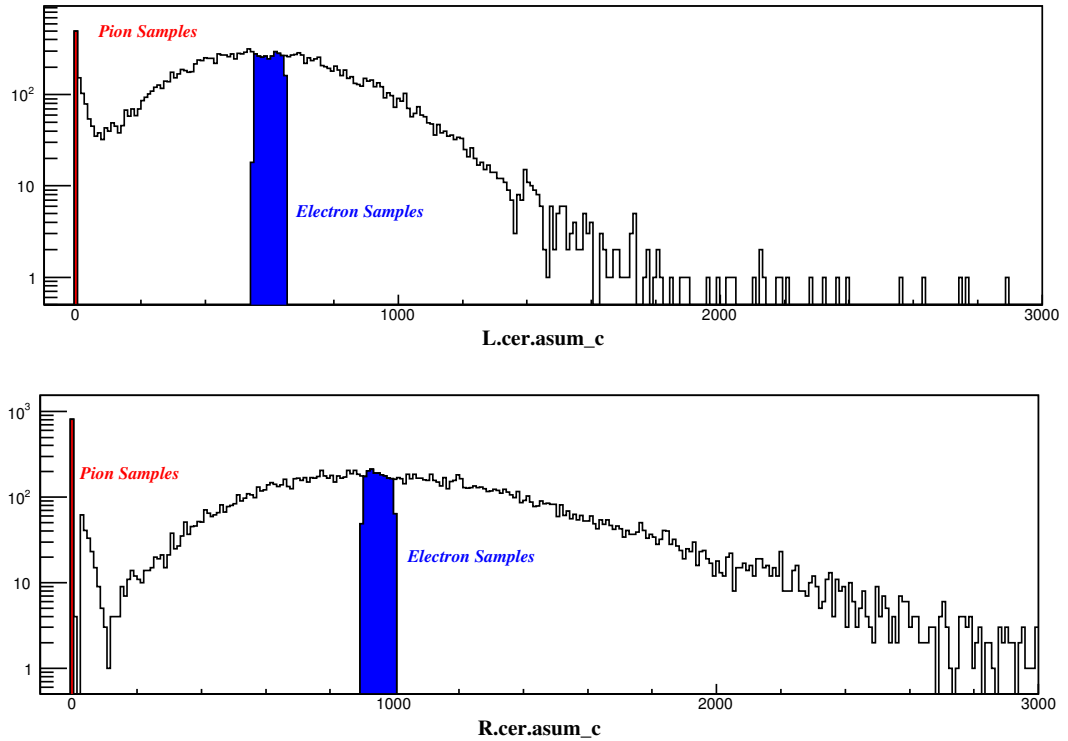
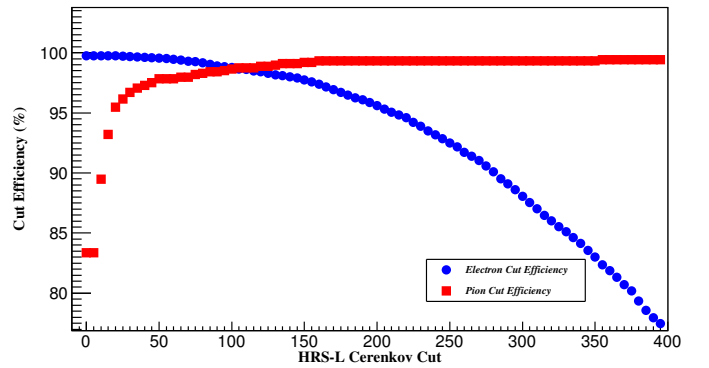
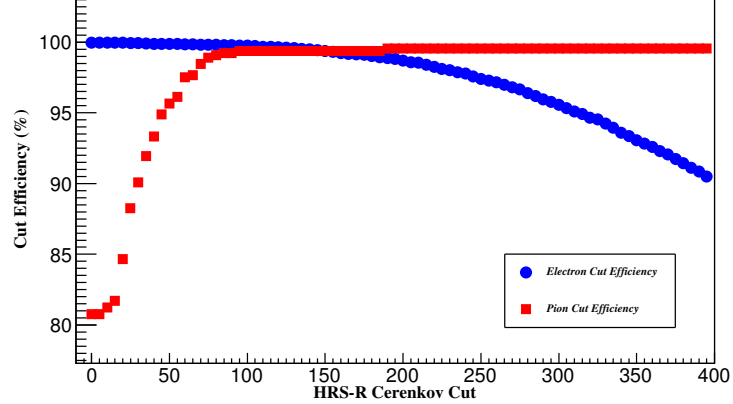


Figure 5: Electron and pion samples from the GC. The x-axis is the sum of calibrated ADC spectra of ten PMTs in the GC in HRS-L (top) or HRS-R (bottom). Electrons were selected by applying cut on the main peak of the spectrum. Pions can not directly create Čerenkov light and they were selected by cutting on low ADC values.

ADC sum, e.g. $L.cer.asum_c \geq 50$ for HRS-L or $R.cer.asum_c \geq 50$ for HRS-R, has already remove most of pions and preserve more than 99% of electrons. The combined cuts on the calorimeter, $E/P \geq 0.5$ and $L.prl2.e \geq 100$ ($R.sh.e \geq 200$), can further remove more than 90% of pions while remaining more than 99% of electrons, shown Fig. 9a and Fig. 9b. In total, on HRS-L (HRS-R), 99.85% (99.62%) of pions are eliminated with these combined PID cuts, while 99.58% (99.86%) of electrons survive after the cuts. Considering the high electrons rates and low pion production for this experiment, one is not required to specifically correct the pion contamination, and the value of $\epsilon_{e-\pi}$ in Eq. (1) was set to one.

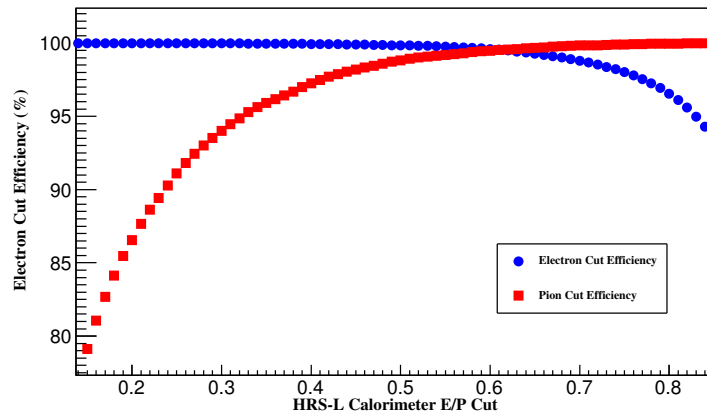


(a) GC cut scan on HRS-L

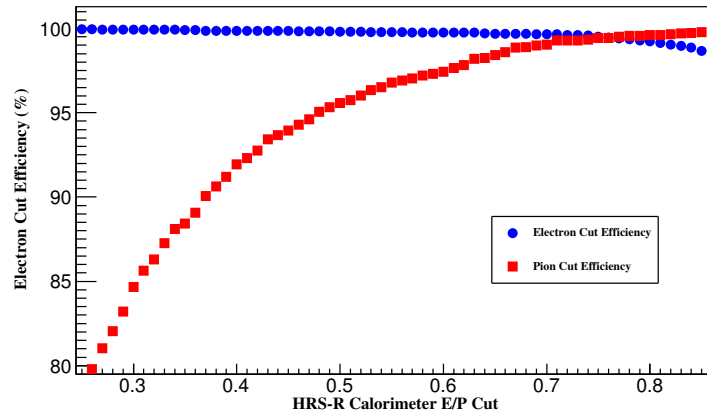


(b) GC cut Scan on HRS-R

Figure 6: Cut scan of the GCs on HRS-L (top) and HRS-R (bottom). The x-axis is the channel number of the GC's ADC sum where the cut applies on. The cut efficiencies of pion (red boxes) and electrons (blue dots) were calculated with Eq. (14) and Eq. (15) by varying the cut on the GC.

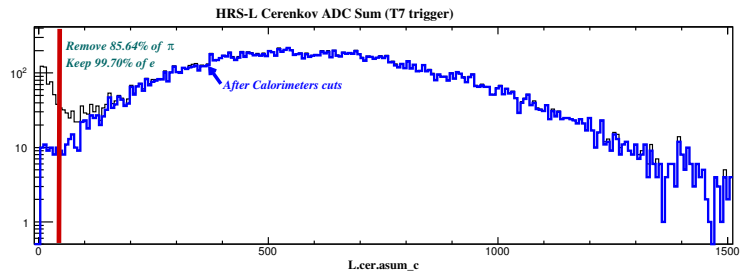
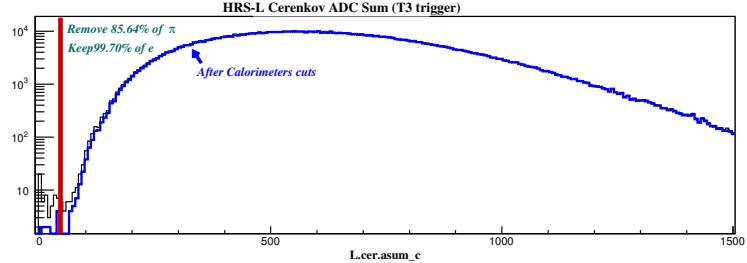


(a) Calorimeter cut scan on HRS-L

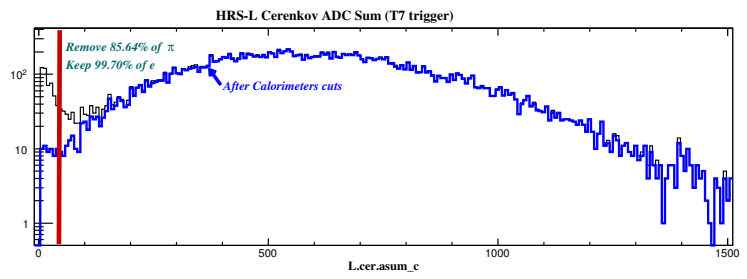
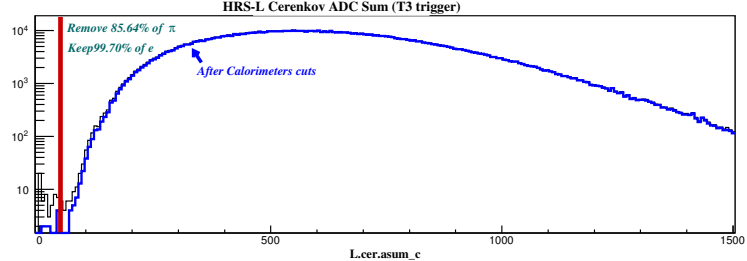


(b) Calorimeter cut scan on HRS-R

Figure 7: Cut scan of the calorimeters on HRS-L (top) and HRS-R (bottom). The x-axis is the channel number of the calorimeter's ADC sum where the cut applies on. The cut efficiencies of pion (red boxes) and electrons (blue dots) were calculated with Eq. (14) and Eq. (15) by varying the cut on the calorimeter.

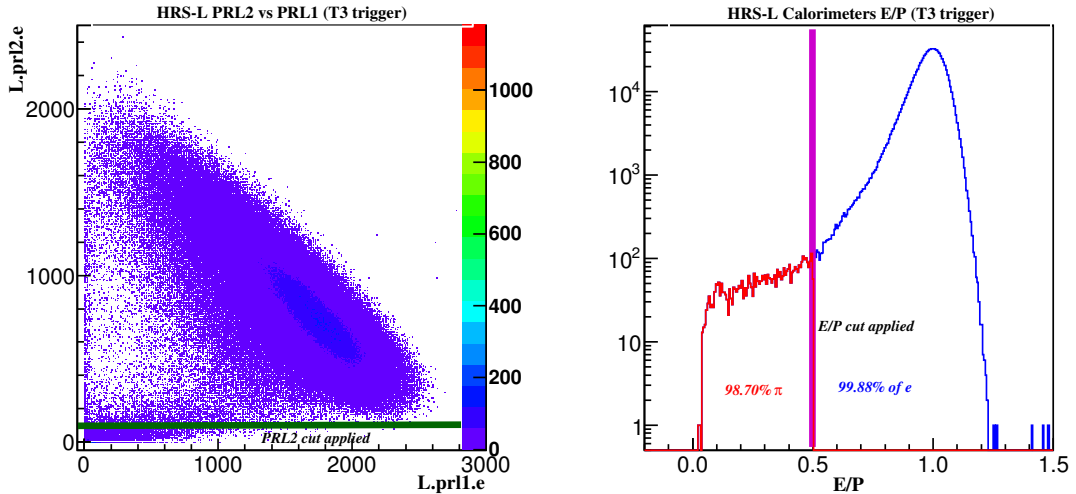


(a) on HRS-L

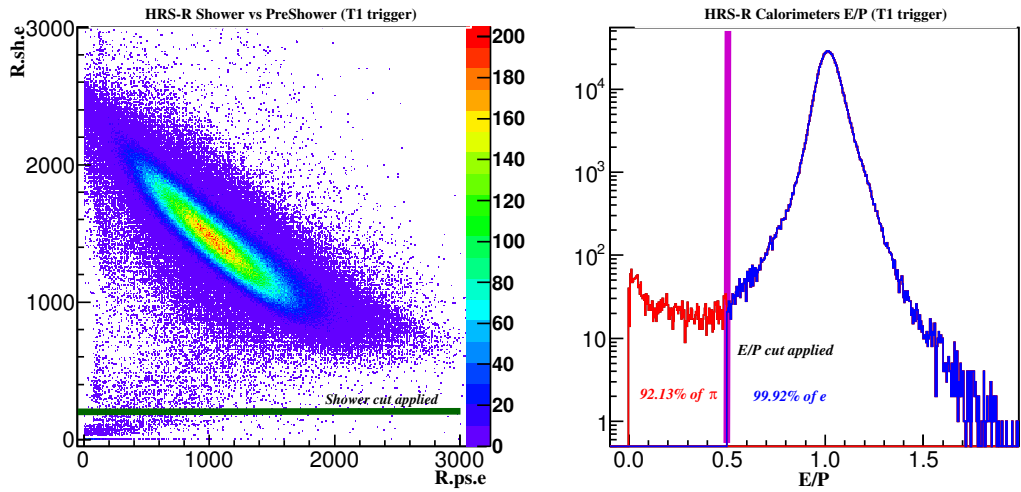


(b) on HRS-R

Figure 8: PID cut on the GCs. In each panel, the top and bottom histograms plot the calibrated ADC sum of events triggered by T1 (T3) and T6 (T7) from HRS-R (HRS-L), respectively. Most of pions have already been rejected in events from T1 and T3 during data taking, so a minimum cut on the GC's ADC spectrum (≥ 50) can further remove the rest of pions.



(a) on HRS-L



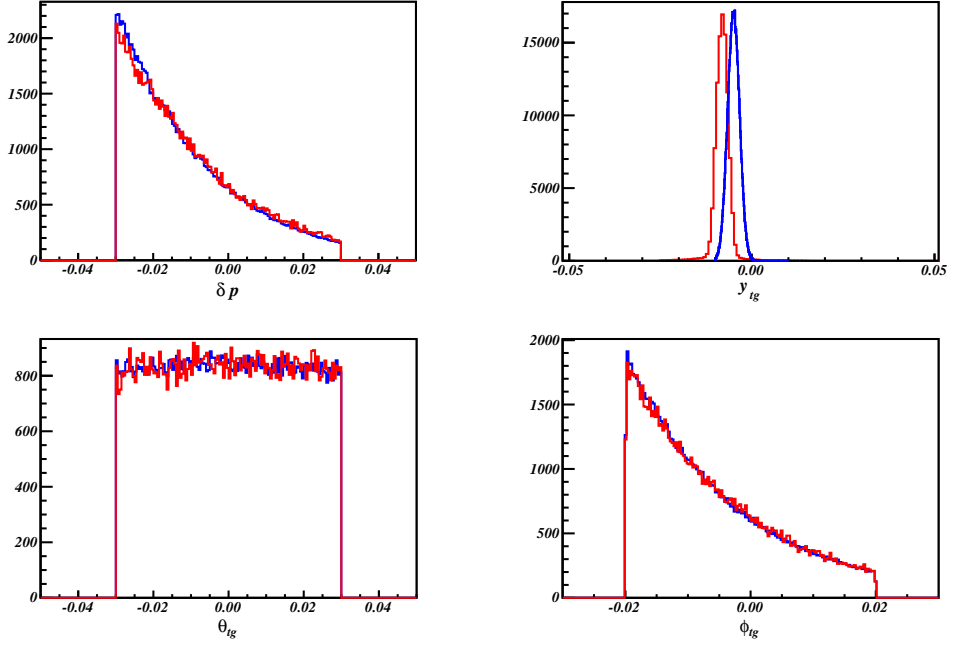
(b) on HRS-R

Figure 9: PID cut on the calorimeters. Most of pions can be removed by the $E/P \geq 0.5$ and the cut on the second layer's ADC spectrum ($PRL2 \geq 100$ or $SH \geq 200$).

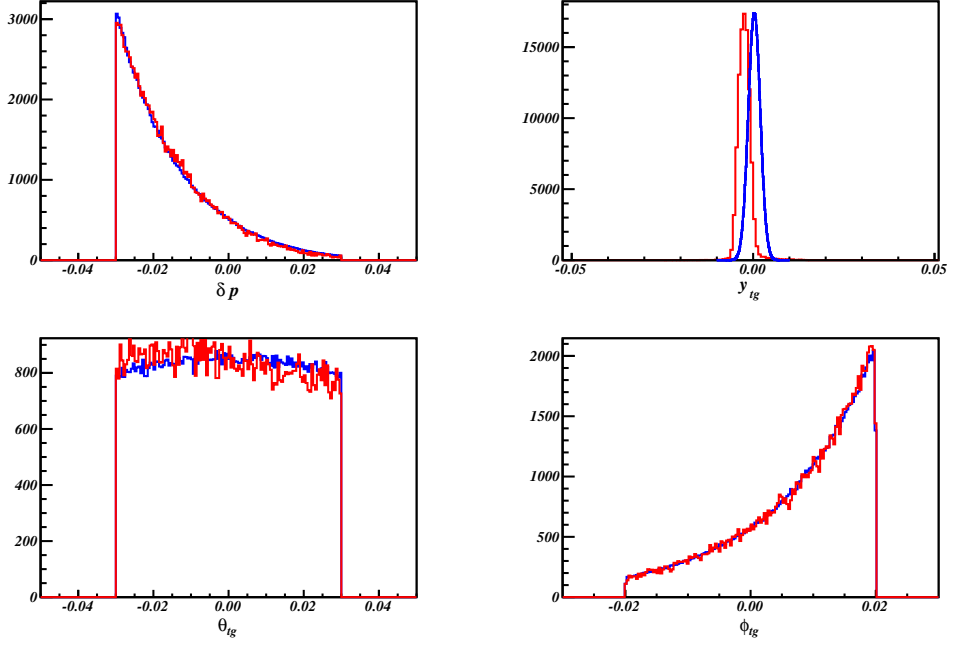
6 Monte Carlo Simulation

The Hall-A Single Arm Monte Carlo simulation tool (SAMC) was designed to simulate the transportation of particles from the target plane to the focal plane. SAMC was originally developed in FORTRAN [3] and then converted into C++ [4]. The beam position, the spectrometer settings, and the information of the target system can be specified in the code to match the experimental settings. A simulated event has its specified values of the incoming energy, the scattered momentum and the scattering angle, which are defined in the target coordinate system and called the target plane quantities. These quantities are randomly generated with uniform distributions, and with these quantities as inputs, each focal plane quantity is calculated by a set of forward transportation functions which are generated by the SNAKE model [5]. After the focal plane quantities are smeared with the resolution of VDCs, another set of backward transportation functions are used to reconstruct the target plane quantities. During these two processes, events inside and outside the HRS acceptance can be individually identified. Before comparing with the experimental data, the distributions of the target plane quantities are weighted by the radiated cross section values of these simulated events which can be calculated with cross section models embedded in the code. In this analysis, a new cross section model and a special treatment of the no-uniform cryogenic targets have been added in SAMC.

There were 20 million events generated for each target in each kinematic setting. Fig. 10 and Fig. 11 compare the distributions of reconstructed target plane quantities between simulated data and experimental data for ^{12}C and ^3He . The histograms for simulation data were weighted by the cross sections calculated by XEMC (see next section and Appendix B). The distribution of the same quantity from these two data sets agree nicely with each other. The distribution of z_{react} for the cryogenic target was simulated with the relative density distribution function extracted with the method discussed in Appendix D.

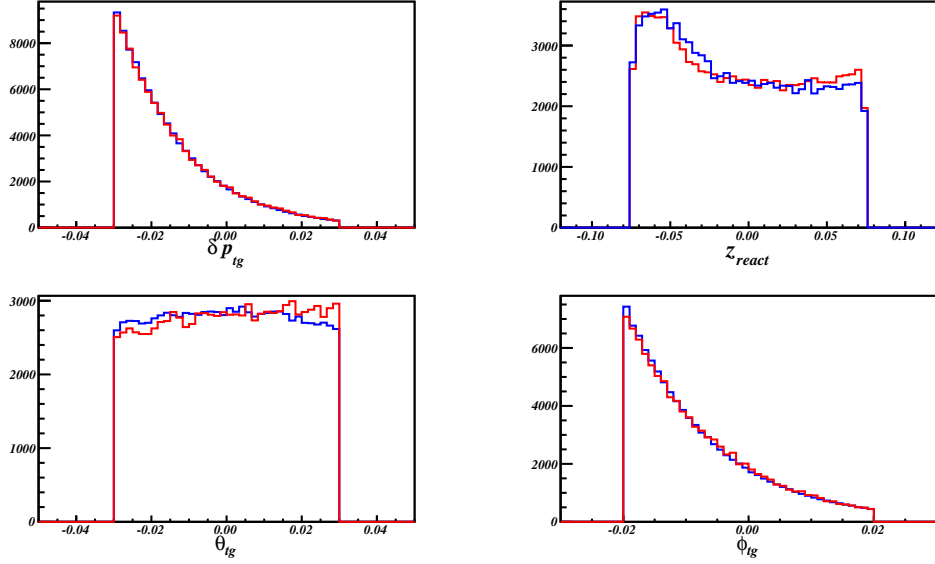


(a) Target plane quantities on HRS-L

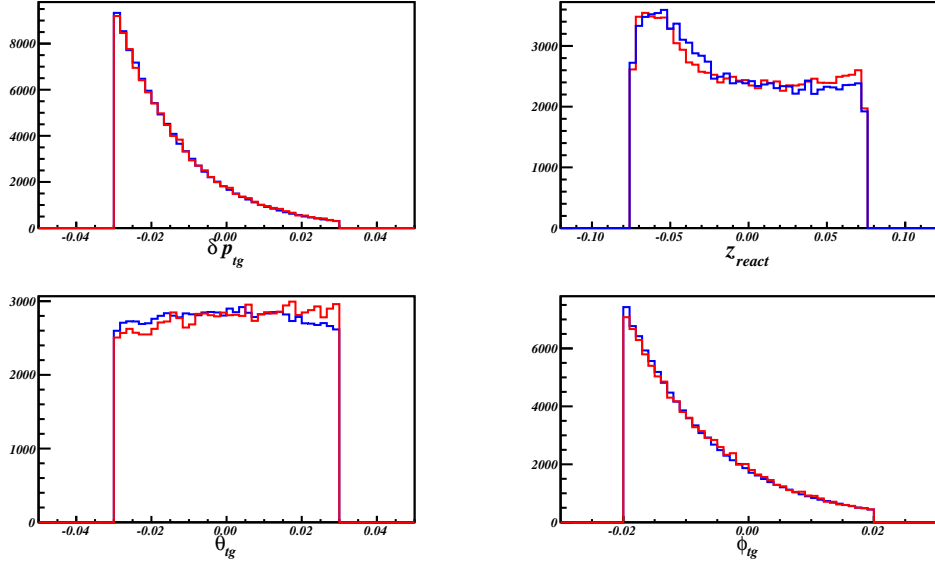


(b) Target plane quantities on HRS-R

Figure 10: Simulation of ^{12}C target plane quantities, where red lines are simulation data from SAMC and blue lines are from the E08-014 data. The offset of y_{tg} between two data is a known issue of SAMC but the offset was too small to affect the acceptance.



(a) Target plane quantities on HRS-L



(b) Target plane quantities on HRS-R

Figure 11: Simulation of ${}^3\text{He}$ target plane quantities, where red lines are simulated data from SAMC and blue lines are the experimental data. Instead of y_{tg} , the z_{react} distribution is given to compare the real density distribution which was simulated with the function fitted from data (Appendix D).

7 Cross Section Model

The inclusive electron scattering cross sections model used in this data analysis is XEMC, a C++ package to compute Born cross sections and radiated cross sections. A brief discussion of the cross section models and radiative correction is given in Appendix B.

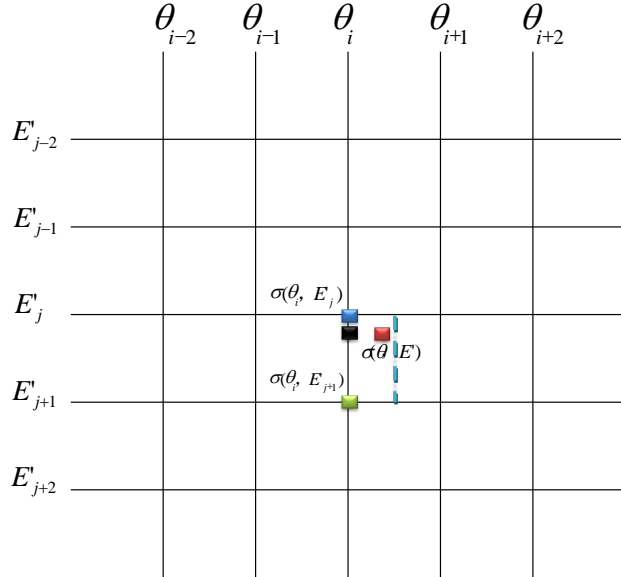


Figure 12: A sketch of cross section lookup tables. $\sigma(\theta, E') \equiv \sigma(\theta_i, E')$ when $\theta_i \leq \theta < (\theta_i + \theta_{i+1})/2$, and $\sigma(\theta, E') \equiv \sigma(\theta_{i+1}, E')$ when $(\theta_i + \theta_{i+1})/2 \leq \theta < \theta_{i+1}$, e.g. from the red point to the black point in this plot. For $E'_j < E' < E'_{j+1}$, the cross section is calculated with the linear relationship given in Eq. (16).

Calculating radiated cross sections with XEMC usually takes very long time. To generate millions of simulated events, cross section look-up tables were generated for each target in each kinematic setting. When generating each table, the range of the scattering angle, $\Delta\theta$, and the scattered energy, $\Delta E'$, were slightly wider than the actual HRS acceptance. $\Delta\theta$ was divided into 200 bins and $\Delta E'$ was also split into bins of 5 MeV. As shown in Fig. 12, the kinematic space for each setting was given as a 2-dimensional lattice where the born cross section and the radiated cross section for each grid, (θ_i, E'_j) , were simultaneously calculated. Since the bin sizes are very fine, for fixed momentum, the cross sections at different angles are considered to be equal within one θ bin, while for a fixed angle, the cross sections are assumed to be proportional to the momentum values inside one E' bin. As illustrated in Fig. 12, for a given event, (θ, E') , the value of θ is replaced by the closest angle bin, e.g. θ_i , and when two momentum bins are specified, e.g. $E'_j < E' < E'_{j+1}$, the cross section value for this event can be calculated with the linear relationship:

$$\sigma(E', \theta) = \sigma(E'_j, \theta^i) - \frac{E' - E'_j}{E'_{j+1} - E'_j} (\sigma(E'_{j+1}, \theta^i) - \sigma(E'_j, \theta^i)). \quad (16)$$

For the same event, the difference between the cross section obtained from the look-up table and the cross section directly calculated from XEMC is less than 0.1%. This method can dramatically reduce the computation time when generating simulation events. Tables were re-generated each time when the model was changed or the experimental details were updated, e.g. the target thickness.

8 Event Selection and Corrections

The ideal way to extract an experimental cross section is to use the scattered electrons with the same values of E_0 , E' and θ . However, although the beam energy can be easily locked at one value,

E' and θ can vary within the acceptance of the spectrometer, and due to the statistical limitation, the cross sections can only be calculated by allowing the values of E' and θ to change within finite ranges, e.g. $\Delta E'$ and $\Delta\Omega$ in Eq. (1). In practice, the experimental data is divided by binning one or more kinematic variables with known bin sizes, and the cross section is evaluated at the center of each bin. The way to choose the binning method, including the acceptance ranges and the bin sizes, requires additional corrections during the cross section extraction.

For the E08-014, the data was binned in E' only, and the cross sections were calculated in each E' bin with the same scattering angle, $\theta = \theta_0$. The determination of the kinematic space, the acceptance correction and the binning correction will be discussed in this section. A list of cuts to select the good electron events is also given.

8.1 Central Momentum and Angle

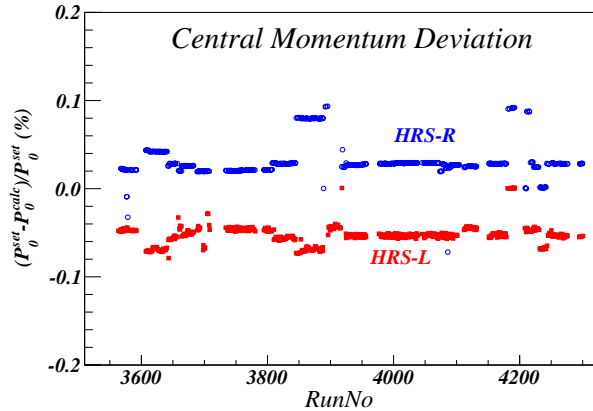


Figure 13: Central momentum deviation, where the blue circles and the red boxes are the deviations of the central momentum on HRS-R and HRS-L, respectively. The x-axis is the run number and the y-axis is the deviation in percentage.

The kinematic space is determined by the central scattered momentum, the central scattering angle, and the acceptance of the HRS. The central momentum was given by the field values of the HRS magnets which were locked at the setting values by the HRS NMR system during the experiment. The off-line calculation gives the absolute value of the central momentum with the magnetic field of the dipole [6]:

$$P_0 = \sum_{i=0}^4 \gamma_i \cdot (10 \cdot B_{dipole}^{NMR})^i, \quad (17)$$

where $\gamma_{1,2,3,4} = (0, 270.2, 0, -0.0016)$ for HRS-L and $\gamma_{1,2,3,4} = (0, 269.8, 0, -0.0016)$ for HRS-R. B_{dipole}^{NMR} is the field reading from the NMR monitor. Fig. 13 shows that the actual central momenta were mostly off by $\pm 3\%$ while few of them were off by $\pm 10\%$. During the cross section extraction, the central momenta were assigned to the calculated values instead of the set values.

The central scattering angle was specified during the experiment by moving the HRS to point at the angle marked on the floor. These floor marks were drawn with respect to the hall center and may not accurately reflect the true values. Moreover, the actual central scattering angle also depends on the offsets between the spectrometer center and the hall center which are different when the spectrometer points at different angles. For some extreme cases, when the spectrometer is moved away from one angle and later moved back to the same value, the actual angles may be different between these two periods.

To obtain the actual central scattering angle each time after the spectrometer was moved, a survey would be performed to correct the errors of the floor marks and to measure the offset between the two centers. Unfortunately, the survey could not be done each time the spectrometers were moved. However, the optics target was surveyed at the beginning of this experiment when both HRSs were set at 25° , and the positions of z_{react} at different angles can be extracted from the data. Combined with the survey reports from earlier experiments which had similar settings, the

RunNo	$\theta_0^{set}(L)$	$\theta_0^{true}(L)$	$\theta_0^{set}(R)$	$\theta_0^{true}(R)$
3565~3656	25.00	25.00	25.00	25.00
3657~3683	21.00	21.03	21.00	21.04
3684~3708	23.00	23.00	23.00	23.01
3735~3891	25.00	24.99	25.00	25.00
3892~3916	—	—	21.00	21.03
3917~4071	28.00	27.98	28.00	27.99
4073~4103	21.00	21.04	28.00	27.99
4112~4179	23.00	23.00	23.00	23.04
4181~4241	25.00	24.98	25.00	25.00
4242~4250	21.00	21.02	21.00	21.03
4251~4299	28.00	27.98	28.00	27.99

Table 3: Scattering angle correction

actual central scattering angles can be calculated with the difference of z_{react} at 25° and at the setting angle ($\Delta z_{react} = z_{react}(\theta_0) - z_{react}(25^\circ)$), as follow:

$$\theta_{tg} = \frac{D_x + x_{sieve} - y_{beam}}{L - x_{beam} \cdot \sin\theta_0^{set} - \Delta z_{react} \cdot \cos\theta_0^{set}}, \quad (18)$$

$$\phi_{tg} = \frac{D_y + y_{sieve} - x_{beam} \cdot \cos\theta_0^{set} + \Delta z_{react} \cdot \sin\theta_0^{set}}{L - x_{beam} \cdot \sin\theta_0^{set} - \Delta z_{react} \cdot \cos\theta_0^{set}}, \quad (19)$$

$$\theta_0^{true} = \arccos \left(\frac{\cos\theta_0^{set} - \phi_{tg} \sin\theta_0^{set}}{\sqrt{1 + \theta_{tg}^2 + \phi_{tg}^2}} \right), \quad (20)$$

where D_x , D_y , x_{sieve} , y_{sieve} and L are given in Table ?? and Table ???. The beam position (x_{beam} , y_{beam}) was locked at (-2.668 mm, 3.022 mm) during the experiment. θ_0^{set} is the central scattering reading from the floor marks and θ_0^{true} is the actual central scattering angle after the correction. As shown in Table 3, the calculation showed that the maximum offset between θ_0^{true} and θ_0^{set} was not larger than 0.04° . The value of θ_0^{true} was calculated for runs taken at each run period when the spectrometer was moved to different positions. The cross sections were calculated with these updated values.

8.2 Acceptance Correction

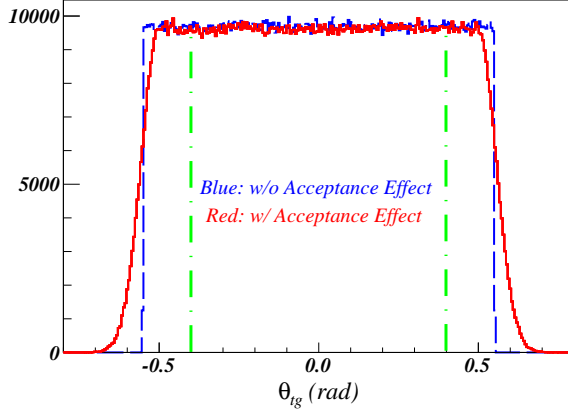


Figure 14: A demonstration of the acceptance effect, where the distribution of θ_{tg} is generated by assuming no cross section weighting effect. The blue line shows that the acceptance is flat when the HRS acceptance is perfect, while the red line demonstrates the slow fall-off of the acceptance edges. Such an effect is mainly due to the geometry of the HRS magnets and also contributed by the resolutions of the VDC tracking and the optics reconstruction. Green lines show the cuts to select the flat acceptance region.

The HRS acceptance includes both the range of momentum dispersion ($\Delta\delta p$) and the total solid angle which is the product of the out-of-plane angle (θ_{tg}) and the in-plane-angle (ϕ_{tg}). For an extended target, the optics reconstructed reaction point along the beam direction (z_{react}) is also affected by the HRS acceptance. These four quantities, called the target plane quantities, are essential to reconstruct the reaction at the target. Due to the geometry of the HRS magnets, the event distributions of these quantities are not cut off immediately at the edge of the acceptance and instead, they fall off relatively slowly with a gaussian tail, as can be seen in Fig. 14. In addition, the resolution of VDC tracking and the accuracy of the optics reconstruction can also smear the distributions of these quantities.

Choosing the right acceptance ranges of the target plane quantities is crucial in order to obtain the correct cross section results. Tight cuts on the target plane quantities were used to select events at the central region of the HRS acceptance. Cutting out the tails on the edges of the focal plane variables also removes multi-scattering events produced inside the spectrometer. The acceptance cuts will be enlarged to increase the statistics of events in one bin, until the cross section results start to deviate from the results calculated with tighter cuts.

However, good events can be incorrectly discarded when one applies the combination cuts of the four target plane quantities to define a valid acceptance region. Such an effect can be corrected by the HRS simulation for each bin:

$$A(E_0, E_i, \theta_0) = \frac{N_{MC}^{gen}}{\Delta E'_{MC} \Delta \Omega_{MC}} / \frac{N_{MC}^i}{\Delta E'_{bin} \Delta \Omega_{EX}}, \quad (21)$$

where $\Delta E'_{bin}$ is the bin size of E' and is fixed in both the simulated data and experimental data, and $\Delta \Omega_{EX}$ is the selected angular acceptance range for the experimental data. N_{MC}^i is the number of simulated events in the i th bin, with the same acceptance cuts used for the experimental events (N_{EX}^i) in this bin. N_{MC}^{gen} is the total number of simulated events without any cuts. $\Delta E'_{MC}$ and $\Delta \Omega_{MC}$ define the full momentum and angular acceptance in the simulation, respectively, and they are slightly larger than the HRS acceptance. Overall, $\frac{N_{MC}^i}{\Delta E'_{bin} \Delta \Omega_{EX}}$ denotes the average number of events in the unit kinematic space which is limited by the HRS geometry, while the other term, $\frac{N_{MC}^{gen}}{\Delta E'_{MC} \Delta \Omega_{MC}}$, gives the average number of events in the unit kinematic space without any spectrometer limitations. Eq. (21) is usually referred to as the acceptance correction.

8.3 Binning Correction

The cross section results were calculated by binning the data on E' . The binning ranges and step sizes are given in the following table:

Kin	3.1	3.2	4.1	4.2	5.0	5.05	5.1	5.2	6.5
E'^{Min}	2.76	2.90	2.71	2.88	2.38	2.52	2.66	2.85	2.70
E'^{Max}	3.05	3.21	3.00	3.19	2.63	2.78	2.94	3.14	2.99
$\Delta E'$	0.01	0.01	0.01	0.01	0.01	0.01	0.01	0.01	0.01

Table 4: E' binning size and range

From Eq. (1), when binning on E' , the cross section in each bin is given as a function of the central scattering angle (θ_0) and the momentum value at the center of the bin (E'_i). However, events in each bin carry different momenta varying from $E'_i - \frac{1}{2}\Delta E'$ to $E'_i + \frac{1}{2}\Delta E'$, while their central scattering angles can deviate from θ_0 within the solid angle, $\Delta \Omega_{EX}$. A bin-centering correction is applied to remove the effect with the simulation data and the cross section model:

$$B(E_0, E_i, \theta_0) = \frac{\sigma_{XEMC}^{rad}(E_0, E'_i, \theta_0)}{\sum_{j \in i} \sigma_{XEMC}^{rad}(E_0, E'_j, \theta_j)}, \quad (22)$$

where $\sum_{j \in i}$ means summation over the radiated cross section values, $\sigma(E'_j, \theta_j)$, of all Monte Carlo events in the i th bin. $\sigma_{XEMC}^{rad}(E'_i, \theta_0)$ and $\sigma_{XEMC}^{rad}(E'_j, \theta_j)$ are calculated from the XEMC model.

8.4 Cuts

In addition to cutting on the binning variable, there are several other cuts which were applied to select good scattered electron events:

1. Cutting on production trigger events (see Appendix A);
2. Removing pulser events generated by EDTM modules;
3. Beam trip cut;
4. Selecting events with only one track in VDCs;
5. Cuts on the focal plane acceptance;
6. Cuts on the target plane acceptance;
7. PID cuts on the GC and the calorimeter.

When the extraction of cross sections involves data from more than one run, the total number of events after the cuts defined above is given by:

$$N_{EX}^i = \sum_r \frac{PS1(3)^r \cdot N_{T_{1(3)}}^r}{LT_{T_{1(3)}}^r}, \quad (23)$$

where r represents the run number and $N_{T_{1(3)}}^r$ is the total number of events from T_1 on HRS-R (T_3 on HRS-L) and recorded by DAQ after cutting out the beam trip. Note that events from each run are individually corrected by the Live-Time ($LT_{T_{1(3)}}^r$) before they are added together.

9 From Yields to Cross Sections

The experimental Born cross section can be calculated from Eq. (1) after applying the acceptance correction (Eq. (21)) and the bin-centering correction (Eq. (22)):

$$\sigma_{EX}^{Born}(E'_i, \theta_0) = A(E'_i, \theta_0) \cdot B(E'_i, \theta_0) \cdot \sigma_{EX}^{rad}(E'_i, \theta_0) \cdot RC(E'_i, \theta_0). \quad (24)$$

Note that the initial electron energy, E_0 , is fixed at 3.356 GeV during this experiment so it is omitted from the equation. The last term is the radiative correction factor:

$$RC(E'_i, \theta_0) = \frac{\sigma_{XEMC}^{Born}(E'_i, \theta_0)}{\sigma_{XEMC}^{rad}(E'_i, \theta_0)}. \quad (25)$$

Extraction of cross sections from Eq. 24 largely relies on the performance of the simulation and the cross section model, which, however, can not be directly examined from the cross section results. Two useful quantities, the experimental yield and the Monte Carlo (MC) yield, can be extracted to directly compare their differences. The experimental yield is written as:

$$Y_{EX}^i = \frac{N_{EX}^i}{N_e \cdot \epsilon_{eff}}, \quad (26)$$

where $\epsilon_{eff} = \epsilon_{trig} \cdot \epsilon_{vdc} \cdot \epsilon_{e_cut}^{GC} \cdot \epsilon_{e_cut}^{calo}$ which are given in Eq. (12), Eq. (13) and Eq. (15), respectively. The MC yield is given by:

$$Y_{MC}^i = \eta_{tg} \cdot \sum_{j \in i} \sigma_{model}^{rad}(E'_j, \theta_j) \cdot \frac{\Delta\Omega_{MC} \Delta E'_{MC}}{N_{MC}^{gen}}. \quad (27)$$

The ratio of the experimental yield to the MC yield should be close to one if the performance of the HRS can be well simulated by the MC data and the XEMC model produces cross sections close to the actual values. The experimental Born cross section from Eq. 24 can be rewritten as:

$$\sigma_{EX}^{Born}(E'_i, \theta_0) = \frac{Y_{EX}^i}{Y_{MC}^i} \cdot \sigma_{XEMC}^{Born}(E'_i, \theta_0), \quad (28)$$

The yield ratio method can largely reduce the bias caused by the choice of different cross section models and Monte Carlo simulation tools. While the experimental yield is completely extracted from the data and remains unchanged, one can iterate the cross section model and apply necessary corrections only on the MC yield until the the yield ratio becomes close to one for all E' bins. Furthermore, the acceptance cuts on the HRS can also be studied by varying the cuts and checking the distribution of the yield ratio as a function of the binning variable. Most of other potential issues, such as junk runs, incorrect input parameters and so on, can also be examined in the yield ratio method.

10 Calculation of Errors

In the cross section extraction package, a new type of variable is defined by a C++ class *XGT2_VAR*, which not only includes the exact value of one quantity but also includes its systematic error and statistic error, respectively. When a new quantity is calculated from the operation of other quantities, all systematic errors and statistic errors from them will be separately combined and carried by this new quantity. Comparing with evaluation of total errors after we exact the cross section values, this step-by-step method has its advantage to avoid mistakes such as miss-counting or multi-counting. The detail explanation of errors calculation and propagation is given as follows.

From Eq.28,

$$\delta^{stat/sys} \sigma_{EX} = \sigma_{EX} \cdot \sqrt{\left(\frac{\delta^{stat/sys} Y_{EX}}{Y_{EX}}\right)^2 + \left(\frac{\delta^{stat/sys} Y_{MC}}{Y_{MC}}\right)^2} \quad (29)$$

10.1 Y_{EX} :

From Eq.26,

$$\delta^{stat/sys} Y_{EX} = Y_{EX} \cdot \sqrt{\left(\frac{\delta^{stat/sys} N_{EX}}{N_{EX}}\right)^2 + \left(\frac{\delta^{stat/sys} N_e}{N_e}\right)^2 + \left(\frac{\delta^{stat/sys} \epsilon_{\pi/e}}{\epsilon_{\pi/e}}\right)^2 + \left(\frac{\delta^{stat/sys} \epsilon_{eff}}{\epsilon_{eff}}\right)^2}, \quad (30)$$

where I always set $\epsilon_{\pi/e} = 1$, and $\epsilon_{eff} = 1$.

10.1.1 Statistic Errors

1. $\delta^{stat} \epsilon_{\pi/e} = 0$
2. $\delta^{stat} \epsilon_{\pi/e} = 0$
3. $\delta^{stat} N_e = 0$
4. N_{EX} : From Eq.7 and $N_{EX} = \sum_r N_{EX}^r$ for all runs, we have:

$$\delta^{stat} N_{EX}^r = N_{EX}^r \cdot \sqrt{\frac{1}{N_{T_i}^r P_{ST_i}} + \left(\frac{\delta^{stat} LT_{T_i}^r}{LT_{T_i}^r}\right)^2}, \delta^{stat} N_{EX} = \sqrt{\sum_r (\delta^{stat} N_{EX}^r)^2} \quad (31)$$

10.1.2 Systematic Errors

1. $\delta^{sys} \epsilon_{\pi/e} = 0.01$
2. $\delta^{sys} \epsilon_{\pi/e} = 0.01$
3. From Eq.5, since the charge is obtained from the average of four BCM monitor outputs (u_1, u_3, d_1 and d_3), the error is also averaged:

$$\begin{aligned} \delta N_e^r &= \sqrt{\frac{(\delta N_e^{r,d_1})^2 + (\delta N_e^{r,d_3})^2 + (\delta N_e^{r,u_1})^2 + (\delta N_e^{r,u_3})^2}{4}} \\ &= \sqrt{\frac{N_e^{r,d_1} + N_e^{r,d_3} + N_e^{r,u_1} + N_e^{r,u_3}}{4}} \\ &= \frac{\sqrt{N_e^r}}{2} \end{aligned}$$

Hence,

$$\delta N_e = \sqrt{\sum_r (\delta N_e^r)^2} = \frac{1}{2} \sqrt{\sum_r N_e^r} = \frac{1}{2} \sqrt{N_e}, \quad (32)$$

where, r means the run number.

4. $\delta^{sys} N_{EX} = N_{EX} \cdot \sqrt{\sum_r (\delta^{sys} LT^r / LT^r)^2}$. Form Eq.7,

$$\delta^{sys} LT_{T_i}^r = LT_{T_i}^r \cdot \sqrt{\frac{1}{N_{T_i}^{Scaler}} - \frac{1}{N_{T_i}^{DAQ} PS_{T_i}}}, \quad (33)$$

where there is one thing that confuses me, which is that whether I should multiply PS_{T_i} in the first term or not. It won't give us problem so far since most of runs have PS equal to one.

10.2 Y_{MC} :

From Eq.27,

$$\delta^{stat/sys} Y_{MC} = Y_{MC} \cdot \sqrt{\left(\frac{\delta^{stat/sys} N_{tg}}{N_{tg}}\right)^2 + \left(\frac{\delta^{stat/sys} \sum_{j \in i}}{\sum_{j \in i}}\right)^2 + \left(\frac{\delta^{stat/sys} N_{MC}^{gen}}{N_{MC}^{gen}}\right)^2}, \quad (34)$$

10.2.1 Statistical Errors

Statistical errors from all three terms are set to zero.

10.2.2 Systematic Errors

1. Form $N_{tg} = \frac{\rho \cdot l \cdot N_a}{A}$, and $\rho_{cor} = \rho \cdot (1.0 - B \cdot I/100)$, there are three terms that can introduce errors: beam current measurement and calculation (δI), accuracy of Boiling Factors (δB), and the accuracy of target thickness measurement ($\delta \rho$). Last term is known but I temporarily set the first two terms to zero. Hence:

$$\delta N_{tg}^{sys} = \frac{\delta \rho}{\rho} \cdot N_{tg} \quad (35)$$

2. $\delta^{sys} \sum_{j \in i} = (\sum_{j \in i}) \cdot \frac{1}{\sqrt{N_{MC}^i}}$, since it is summarizing the cross section values of MC events (N_{MC}^i) in one bin.
3. $\delta^{sys} N_{MC}^{gen} = \sqrt{N_{MC}^{gen}}$. I generated $2 \cdot 10^7$ events for cryogenic targets and $5 \cdot 10^6$ for foil targets.

10.3 Systematic Table

Source	Scale	Relative	$\delta\sigma/\sigma$	Comment
Trigger Efficiency		$<1.0\%$		
Tracking Efficiency		$<1.0\%$		
GC Efficiency		$<1.0\%$		
Calo Efficiency		$<1.0\%$		
Dead Time		$<0.4\%$		
Pion Contamination (PID)				
Acceptance Correction				
Bin-Centering Correction		$<1.0\%$		
Radiative Correction				
Coulomb Correction				
HRS Momentum		0.02%		
HRS Angle		$<0.5\text{mrad}$		
Beam Energy		0.05%		
Beam Charge		$<1.0\%$		
Target Density				
Target Boiling				
Dummy Subtraction				
Total				

Table 5: E08-014 systematic error table

10.4 Systematic Errors in Cross Section Ratio

The spread-out formula of the experimental differential cross section is given as:

$$\sigma_{EX} = \frac{Y_{EX}}{Y_{MC}} \sigma_{XEMC} = \frac{N_{EX}}{N_e \cdot \epsilon_{eff}} \frac{N_{MC}}{\eta_{tg} \cdot \sum_{j \in i} \sigma_{model}^{rad}(E'_j, \theta_j) \cdot \Delta\Omega_{MC} \Delta E'_{MC}} \cdot \sigma_{XEMC}. \quad (36)$$

To decompose each term, we have:

$$\sigma_{EX} = N_{EX} \cdot N_e^{-1} \cdot \epsilon_{eff}^{-1} \cdot (N_{MC})^{-1} \cdot \eta_{tg}^{-1} \cdot \left(\sum_{j \in i} \sigma_{model}^{rad}(E'_j, \theta_j) \right)^{-1} \cdot \sigma_{XEMC} \cdot (\Delta\Omega_{MC} \Delta E'_{MC})^{-1}. \quad (37)$$

Now let's sort out the sources of the systematic error for the cross section:

$$\delta\sigma_{EX} = \delta N_{EX} \oplus \delta N_e^{-1} \oplus \delta \epsilon_{eff}^{-1} \oplus \delta (N_{MC})^{-1} \oplus \delta \eta_{tg}^{-1} \oplus \delta \left(\sum_{j \in i} \sigma_{model}^{rad}(E'_j, \theta_j) \right)^{-1}, \quad (38)$$

where \oplus stands for a quadric sum between two uncorrelated errors, e.g. $\delta_1 \oplus \delta_2 = \sqrt{(\delta_1)^2 + (\delta_2)^2}$. δN_e^{-1} is calculated with Eq. 32, and $\delta (N_{MC})^{-1}$ is determined by how many events have been simulated. We can further decompose rest of terms:

- The number of experimental events in each bin:

$$\delta N_{EX} = \delta \overline{LT}^{-1} \oplus \delta P_0^{HRS} \oplus \delta \theta_0^{HRS} \oplus \delta E_0^{beam}, \quad (39)$$

where \overline{LT}^{-1} is the quadric sum of the live-time values for all runs in the same setting, defined by Eq. 7. Three other terms are quoted from Table 5.

- Efficiency:

$$\delta \epsilon_{eff} = \delta \epsilon_{eff}^{tracking} \oplus \delta \epsilon_{eff}^{trigger} \oplus \delta \epsilon_{eff}^{GC} \oplus \delta \epsilon_{eff}^{EC} \oplus \delta \delta \epsilon_{eff}^{PID}. \quad (40)$$

The value of each term is given in Table 5.

- Target areal density:

$$\delta \eta_{tg} = \delta \rho \oplus \delta Boiling, \quad (41)$$

where $\delta \rho$ is the uncertainty of the target density, $\delta Boiling$ is the uncertainty of the target boiling correction. The value of each term is given in Table 5.

- Model and corrections:

$$\delta \left(\sum_{j \in i} \sigma_{model}^{rad}(E'_j, \theta_j) \right) = \delta RadCorr \oplus \delta BinCorr \oplus \delta CoulombCorr \oplus \delta AccCorr, \quad (42)$$

where $RadCorr$, $BinCorr$, $CoulombCorr$ and $AccCorr$ denote the radiation correction, bin-centering correction, Coulomb correction and acceptance correction, respectively, while their corresponding errors are listed in Table 5.

Now, the cross section ratio between two targets is given as:

$$R = \frac{\sigma_{EX}^{\#1}}{\sigma_{EX}^{\#2}}, \delta R = \sigma_{EX}^{\#1} \oplus \sigma_{EX}^{\#2}. \quad (43)$$

Since the cross sections of two targets are taken with both the same HRS with the same kinematic settings, uncertainties related to HRS and beam are all canceled. The efficiency-uncertainties, except $\delta \epsilon_{eff}^{trigger}$, are also canceled. Since the data is binned with the same method and the same simulation tool is used, $BinCorr$ and $AccCorr$ are expected to be the same between two targets, unless they have different target lengths, e.g. one is a foil and the other is a long target. Rest of terms are expected to be different between two targets and hence can not be canceled, which lead to:

$$\begin{aligned}
\delta R = & [\delta(\overline{LT}^{\#1})^{-1} \oplus \delta(\overline{LT}^{\#2})] \\
& \oplus [\delta(N_e^{\#1})^{-1} \oplus \delta(N_e^{\#2})] \\
& \oplus [\delta(N_{MC}^{\#1})^{-1} \oplus \delta N_{MC}^2] \\
& \oplus [\delta(\epsilon_{eff}^{trigger-\#1})^{-1} \oplus \delta\epsilon_{eff}^{trigger-\#2}] \\
& \oplus [\delta(\rho^{\#1})^{-1} \oplus \delta\rho^2] \\
& \oplus [\delta(Boiling^{\#1})^{-1} \oplus \delta Boiling^{\#2}] \\
& \oplus [\delta(RadCorr^{\#1})^{-1} \oplus \delta RadCorr^{\#2}] \\
& \oplus [\delta(CoulombCorr^{\#1})^{-1} \oplus \delta CoulombCorr^{\#2}] \\
& \oplus [\delta(AccCorr^{\#1})^{-1} \oplus \delta AccCorr^{\#2}].
\end{aligned}$$

References

- [1] P. Solvignon-Slifer, E08-014 BCM calibration report, 2012.
- [2] D. Meekins, E08-014 target report, http://hallaweb.jlab.org/experiment/E08-014/analysis/HallA_Target_Configuration_Apr2011.pdf, 2011.
- [3] A. Duer, Single Arm Monte Carlo for Polarized 3He experiments in Hall A v.0.2, <http://hallaweb.jlab.org/publications/Technotes/files/2001/01-004.pdf>, 2002.
- [4] H. Yao, Ph.D Thesis, Temple University , 2011.
- [5] J. LeRose, HRS transportation functions.
- [6] J. Alcorn *et al.*, Nucl. Instrum. Meth. **A522**, 294 (2004).